ELSEVIER

Journal of Power Sources 97–98 (2001) 174–180

JOURNAL OF POWER SOURCES

www.elsevier.com/locate/jpowsour

Raman microscopy as a quality control tool for electrodes of lithium-ion batteries

Jan-Christoph Panitz[1], Petr Novák[*]

Paul Scherrer Institute, Laboratory for Electrochemistry, CH-5232 Villigen, PSI, Switzerland

Received 20 June 2000; accepted 30 December 2000

Abstract

The Raman mapping technique is shown to be suitable for quality control of both positive and negative electrodes for lithium-ion batteries. An analysis of the spectral features observed at a multitude of locations on the electrode surface allows a distribution of band parameters to be obtained that is unique for a given kind of electrode. It is shown that band positions, linewidths, and intensity ratios can be employed as descriptors of the distribution. Such distributions can in turn be used to generate a fingerprint for a particular kind of electrode.

Keywords: Raman microscopy; Carbon; Lithium cobalt oxide; Rechargeable lithium-ion batteries; Electrode characterization

1. Introduction

Several tens of millions of lithium-ion cells are monthly manufactured worldwide. As the component quality is crucial for the market success of the final product, producers are still searching for faster and more reliable component characterization tools. In both electrodes of a lithium-ion battery carbonaceous materials are used. For an analysis of the structural properties of carbons, Raman spectroscopy is well suited [1–6]. Moreover, the electroactive oxides used in positive electrodes can readily be characterized by the same technique [7,8]. Because the surfaces of the electrodes are not homogeneous and typically reveal one or two types of carbon and/or an oxide, a binder, and occasionally an additive, a lateral resolution at the electrode surface corresponding to a typical particle size of a few millimeters must be achieved so that each component may be characterized individually. The required resolution can be achieved with surface mapping techniques based on Raman microscopy. In the present work we wish to demonstrate that the Raman mapping technique is suitable for quality control of battery electrodes. In addition, such investigations enhance the value of in situ Raman studies of battery electrodes in general [9–11].

2. Experimental

Commercial electrode sheets for lithium-ion batteries were used as received. The samples were cut to appropriate sizes and placed under the microscope. Raman microscopy was performed with a confocal Raman microscope (LabRam, Jobin Yvon) using excitation from an external Kr^+-ion laser operated at an emission wavelength of 530.9 nm. Raman spectra were recorded in the spectral range of 250–4100 cm^{-1}. Laser power at the sample at a spot of about 10 μm^2 was limited to about 1–3 mW. Lines from a neon lamp (Pen-Ray, Oriel) were used for calibration of measured band positions, which are accurate to ± 3 cm^{-1}. Further details of the set up has already been published [12].

For surface mapping, the pinhole diameter was adjusted to 200 μm. Depending on the microscope objective used, this diameter corresponds to a lateral resolution of about 2 μm (magnification 100×) or about 4 μm (magnification 50×). Recorded Raman maps consist of at least 12×12 points, each point representing a Raman spectrum with a spectral resolution of 10 cm^{-1}. The data obtained were analyzed using the software supplied by the manufacturer of the Raman microscope. In addition, the software package Origin (version 5.0, Microcal Software, Inc.) was used for analysis of the spectral data.

[*] Corresponding author. Tel.: +41-56-310-2457; fax: +41-56-310-4415.
E-mail address: petr.novak@psi.ch (P. Novák).
[1] Present address: Chemetall GmbH, Trakehner Strasse 3, DE-60487 Frankfurt am Main, Germany.

0378-7753/01/$ – see front matter
PII: S0378-7753(01)00679-6

3. Results and discussion

3.1. Cathode sheets

Four different types of cathode sheets were investigated using Raman microscopy. In the following, the features observed on a typical cathode sheet are described, using an arbitrarily selected Raman spectrum. From Fig. 1, it can be seen that Raman spectroscopy is able to differentiate the main components of practical cathode sheets. The bands observed are associated with the carbon additive (indicated by D, G, and 2D) [1,5], and with the first-order modes of $LiCoO_2$ (A_{1g}, 596 cm^{-1}, E_g, 486 cm^{-1}) [13]. The A_{1g}-mode is particularly useful for a description of the properties of $LiCoO_2$. Only oxygen atoms are involved in this vibrational mode. It had already been shown that the band position of this mode varies with the amount of lithium present in the crystallite [13]. This implies that the A_{1g}-mode frequency depends on the Li/Co atomic ratio in the material. From the well-developed signals in the wavenumber range 900–1200 cm^{-1} (Fig. 1) that are associated with second-order modes of $LiCoO_2$, we infer that the manufacturer of this particular electrode used a well-crystallized pigment, whereas the spectral features due to the carbon matrix indicate that pyrolytic carbon was used as the conductive filler.

The arrows in Fig. 1 show the bands used in the following to illustrate the distribution of $LiCoO_2$ and pyrolytic carbon over the cathode surface, which is shown in Fig. 2 for this particular electrode sheet. For the $LiCoO_2$, the A_{1g}-band is used, whereas for the carbon component, the 2D-band is employed, since the first-order bands of carbon overlap with the second-order features of $LiCoO_2$, which may interfere with a faithful representation of the component distributions. On the gray scale employed, lightness is proportional to the ratio A, defined as $A = I(LiCoO_2, A_{1g}\text{-mode})/I(\text{carbon, 2D-band})$. Therefore, dark areas correspond to spots with low or zero $LiCoO_2$ content, whereas the white/light gray zones correspond to areas with higher amounts of $LiCoO_2$. The map presented in Fig. 2 illustrates how Raman microscopy can be employed to examine the distribution of carbon on the electrode surface. In this case, we find that carbon is located mostly between the $LiCoO_2$ particles, and thus provides conductive paths between the metal oxide particles.

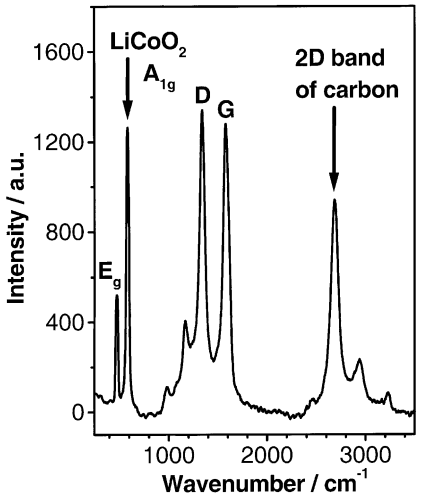

Fig. 1. Typical Raman spectrum recorded on a cathode sheet.

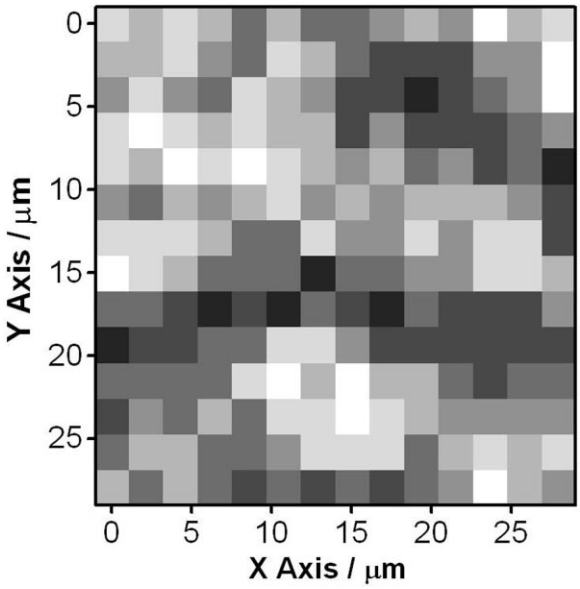

Fig. 2. Distributions of $LiCoO_2$ and carbon on an arbitrarily selected site of the cathode sheet sample KB2, represented as a map of band intensity ratios A recorded with Raman microscopy. The ratio A is defined as $I(LiCoO_2, A_{1g}\text{-mode})/I(\text{carbon, 2D-band})$. Lightness corresponds to higher values of A, and therefore to higher $LiCoO_2$ levels.

By further analysis of the set of Raman spectra recorded for each sample one can calculate the band position and linewidth at each point of the map where signals of $LiCoO_2$ are recorded. In this way a fingerprint of an electrode sheet is obtained. Using the band positions and linewidths of the A_{1g}-mode of $LiCoO_2$ as descriptors, such an analysis was performed for the four different cathode sheets investigated. In addition, an average Raman spectrum was calculated, taking into account all spectra recorded. An analysis of this average spectrum should yield results equivalent to those that might have been obtained using conventional Raman spectroscopy. Our results are presented in the following Figs. 3–5, and a comparison is made between results obtained by both methods.

In Fig. 3, the average spectra calculated for the cathode sheets are presented. The four spectra are normalized with respect to the magnitude of the strongest band of carbon. A comparison of the relative magnitudes of the Raman bands of $LiCoO_2$ with those of carbon reveals striking differences in the amounts of carbon present at the surface. However, it cannot be excluded that the porosity of the carbon employed in these electrodes may vary from sample to sample, hence the efficiencies of the Raman scattering process for the carbon component may be different in different samples

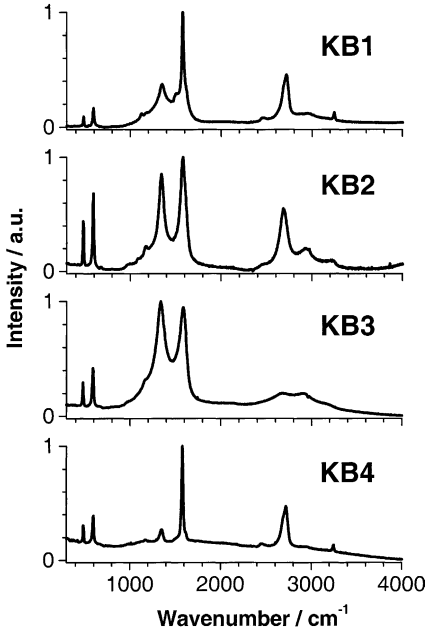

Fig. 3. Average Raman spectra of the four cathode sheet samples, calculated by averaging all spectra recorded for the respective Raman map.

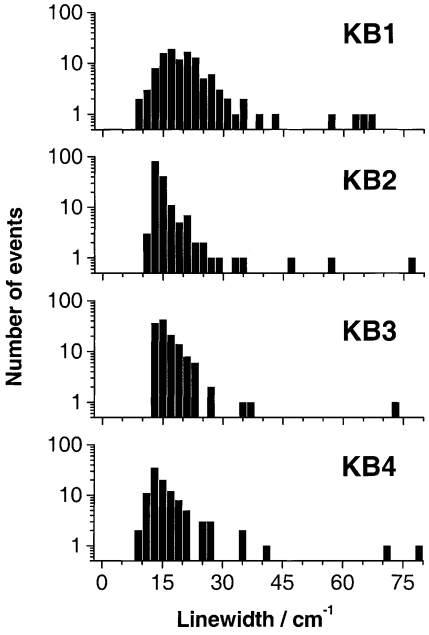

Fig. 5. Distributions of calculated linewidths of the A_{1g}-mode of $LiCoO_2$ for four different cathode sheets.

of cathode sheets, which makes a direct and quantitative comparison of intensity ratios uncertain. Nevertheless, a ranking of the relative amounts of carbon and $LiCoO_2$ present at the electrode surfaces appears to be legitimate. Thus, the highest amount of $LiCoO_2$ is found in sample KB2, while samples KB3 and KB4 take second and third place, and the lowest amount of $LiCoO_2$ is found in sample KB1. The intensity ratio $I(E_g)/I(A_{1g})$ calculated for the $LiCoO_2$ component varies between 0.3 (KB1) and 0.5 (KB2). Very similar values are obtained for the other samples investigated (KB3: 0.38; KB4: 0.39). It has been suggested that the intensity ratio $I(E_g)/I(A_{1g})$ is related to the orientation of the crystallites at the surface [13], but no further details about the correlation between the orientation and intensity ratio were reported.

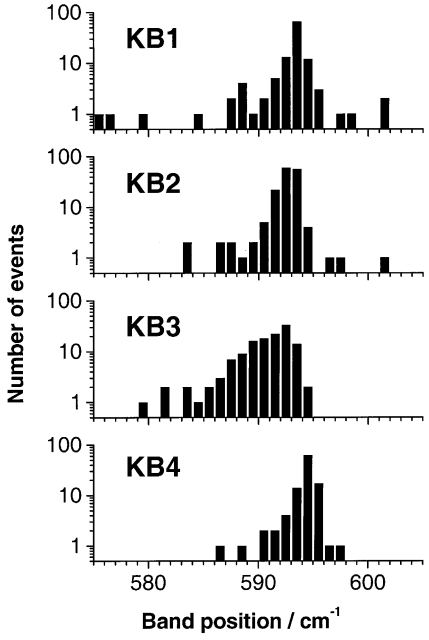

Fig. 4. Distributions of calculated band positions of the A_{1g}-mode of $LiCoO_2$ for four different cathode sheets.

The spectra shown in Fig. 3 also yield information about the type of carbon employed when formulating the cathode mass. The carbon in cathode sample KB1 appears to contain a well-graphitized fraction, in view of the high intensity and small linewidth of the G-band signal. From the rather larger linewidth of the D-band, to the contrary, we infer that less highly graphitized carbon is also present in the KB1 cathode. The carbon bands found for samples KB2 and KB3 are similar to those typical for disordered carbon. Such a carbon material results from the pyrolysis of polymeric precursors and has domains less-ordered than those of graphite [2,6]. The spectral features of the carbon bands observed for the samples KB2 and KB3 are similar, but the intensity ratio $I(D)/I(G)$ is higher in the case of sample KB3. According to the literature [1], this observation can be interpreted by assuming that less-ordered carbon (possibly heat-treated at a lower temperature) is used in the formulation of cathode KB3. This interpretation is supported by the additional observation that the second-order bands of carbon show sharp features in the Raman spectrum of sample KB2, whereas rather broad bands are observed in the averaged Raman spectrum of sample KB3. The most highly graphitized carbon is present in the sample KB4, according to the low intensity ratio $I(D)/I(G)$ and the small linewidth.

Thus, although we do not know the sources of the carbon materials employed by the manufacturers of the cathodes, some valuable information on the components of the cathode bands were obtained. It may be inferred from the results discussed above that in the case of sample KB1, a mixture of at least two carbon materials has been used, whereas one major type of carbon has been used in each of the other samples.

The results discussed above could actually have been obtained as well with conventional Raman spectroscopy. However, further analysis of the information contained in the Raman map may reveal other, more subtle differences between the cathode sheets investigated. Fig. 4 shows histograms characterizing the distributions of the band positions of the A_{1g}-mode for the given set of cathode sheets. Each histogram gives the number of band positions located within a defined wavenumber range. The size or interval of this wavenumber range is 1 cm^{-1} for every histogram included in Fig. 4. Such histograms are very useful representations of Raman spectroscopic data, as will be outlined in the following. When discussing the results shown in Fig. 1, it had been stated that the band position of the A_{1g}-mode depends on the atomic ratio Li/Co in the $LiCoO_2$ material. Therefore, it would be very useful to obtain a precise estimate of this band position. The Raman microscope employed in this work is equipped with a dispersive spectrograph. One of the few disadvantages of such a device is the low precision in band positions it yields, especially when results are compared that have been obtained at different spectral positions of the grating. The band positions listed in Table 1 clearly show that rather large differences in band position are obtained for the set of four samples. In view of what had just been pointed out, it will be difficult to decide whether the differences found are due to a different stoichiometry of $LiCoO_2$ or are artifacts arising from the calibration. The best practical solution would be that of investigating all samples at constant position of the grating, i.e. without moving the grating in between measurements. Where this is not possible, another approach is needed. Thus, instead of obtaining a precise band position, a distribution of band positions could be calculated. When the total number of spectra is sufficiently large (>100), the distribution obtained should be the same, irrespective of the orientation of the cathode under investigation. The results presented in Fig. 4 illustrate this approach. By the use of a logarithmic scale for the ordinate, small contributions to the histogram have been enhanced in the representation. It turns out that the cathodes investigated differ, both in the wavenumber range where band positions are found, and in the shape of the distribution. The distribution of band positions found when analyzing the Raman data of cathode KB1 is broad and approximately symmetric. A rather symmetric distribution is obtained as well for the cathode KB2, but the wavenumber interval within which signals of the A_{1g}-mode of $LiCoO_2$ have been detected is narrower than for the sample KB1. Both cathode samples have very similar average band positions (Table 1). In contrast, the distribution curve of cathode KB3 is displaced towards lower wavenumbers, and the distribution is less symmetric. The distribution curve of sample KB4 has the smallest range of band positions among all cathodes investigated.

Similar calculations can be performed on the linewidth of this band, as shown in Fig. 5. Again, for each cathode a different pattern of distribution of the linewidths is obtained. A rather symmetric distribution of linewidths is found for sample KB1. For the other cathodes, the distribution is less symmetric, and the maxima in the distribution are shifted to lower linewidths. Contributions to the distribution which are associated with rather large linewidths are found for all cathodes, but the lower cut-off linewidths are quite different. Using the combination of these two descriptors, it is possible to unambiguously discriminate between different electrode sheets.

The average band position of the A_{1g}-mode listed in Table 1 merits some discussion too. Such an average can be calculated in different ways, using different weighting strategies. Here, we have used two approaches. By averaging over all band positions and linewidths calculated in the Raman map, a number-weighted average is obtained, while the intensity of the A_{1g}-mode, which may differ considerably between different locations of the Raman map, is not taken into account in this case. In contrast, by calculating the band position and linewidth for the average spectra displayed in Fig. 3, an intensity-weighted average is obtained. A comparison of these values provides information about the symmetry of the distribution. In addition, by comparing the average values one can deduce the origin of the major contribution to the distribution. As an example, the samples

Table 1
Average band positions and linewidths (both in cm^{-1}) of the A_{1g}-mode of $LiCoO_2$ for the four cathode sheets investigated

Sample	Band position, number-weighted[a]	Band position, intensity-weighted[b]	Linewidth, number-weighted[a]	Linewidth, intensity-weighted[b]	Number of spectra included
KB1	592.9 ± 3.7	593.2 ± 0.2	21.5 ± 9.8	18.8 ± 0.6	115
KB2	592.5 ± 1.8	593.1 ± 0.1	15.8 ± 7.3	12.2 ± 0.2	160
KB3	590.6 ± 2.6	590.2 ± 0.1	16.9 ± 6.1	17.1 ± 0.3	132
KB4	594.3 ± 1.4	593.8 ± 0.2	17.6 ± 11.6	16.3 ± 0.5	105

[a] Values calculated using data from the Raman map. The number after the ± sign is the standard deviation calculated for the distribution.
[b] Values calculated using curve fitting of the average spectra. The number after the ± sign represents the error inherent in this calculation.

KB2 and KB3 are compared. For the sample KB2, the intensity-weighted value is larger than the value obtained from the number-weighted distribution, whereas the reverse is observed for sample KB3. The interpretation can be offered that the band positions at large wavenumbers contribute more to the total intensity found in the Raman map. It should be noted that this effect is not very strong in our cathode samples. However, from the values listed in Table 1 it can be concluded that the locations on the map where signals of $LiCoO_2$ with a higher wavenumber and/or lower linewidth are present provide a larger contribution to the total intensity recorded for the A_{1g}-vibrational mode on the map.

3.2. Anode sheets

Four different anodes were investigated using Raman mapping techniques. A typical result is shown in Fig. 6, where the bright-field optical image (top part) is compared to the Raman map subsequently recorded at the same site. The bottom part of Fig. 6 represents a map constructed from the intensity ratios R of the carbon bands, defined as $R = I(\mathrm{D})/I(\mathrm{G})$. We wish to stress that for a Raman map recorded at each particular site, differences in the Raman spectra can be related to the morphology of the electrode. For example, in the area where dark spherical mesocarbon microbeads (MCMB) particles are seen in the video micrograph, the intensity ratio R recorded in the Raman map is higher. Lower values of this ratio are observed at locations where the video micrograph shows particles of more highly graphitized carbon, which are more reflective to the light. Tuinstra and Koenig [1] reported that for carbons a relation exists between the correlation length L_a (derived by analysis of X-ray data) and the spectroscopically derived ratio R. The expression used here for this relation is

$$L_a = \frac{1}{[I(\mathrm{D})/I(\mathrm{G})] \times 22.82/100}\,\mathrm{nm}$$

L_a is a measure of the structural order present in the plane of the graphene sheets in carbon materials. In the following, we discuss the results obtained for the four different anode sheets investigated in terms of this parameter.

Fig. 7 shows the average Raman spectrum of each anode sheet, as calculated by averaging all data points of the Raman map. The spectra are normalized with respect to the magnitude of the carbon G-band. From an inspection of Fig. 7, it is evident that the Raman spectrum obtained for the sample AB1 differs from the other spectra (AB2–AB4) included in Fig. 7. The Raman spectra of samples AB2–AB4 appear to be rather similar, according to the averaged

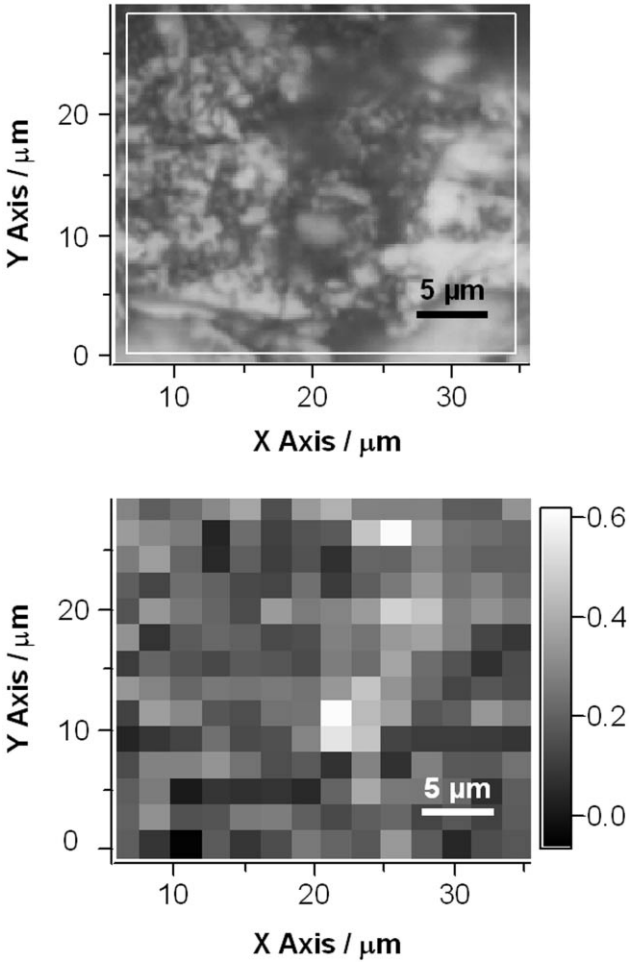

Fig. 6. Video micrograph of anode sheet AB2 (top) and a Raman map of the intensity ratio $I(\mathrm{D})/I(\mathrm{G})$ (bottom) taken at the same site indicated by the white frame in the micrograph. The bright-field image shows the presence of MCMB particles at locations with higher value of the intensity ratio $I(\mathrm{D})/I(\mathrm{G})$, which is a general descriptor of the order present in the plane of the graphene sheets.

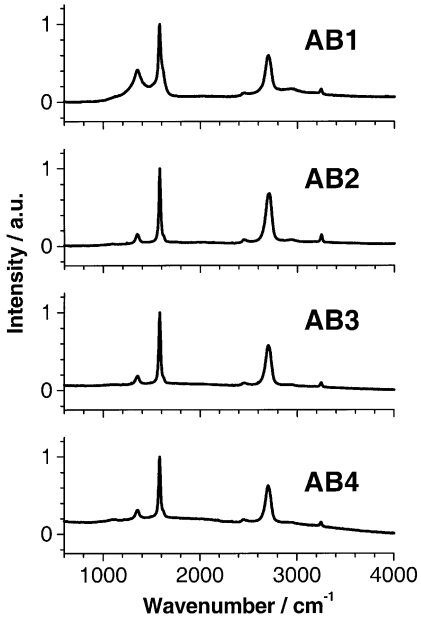

Fig. 7. Average Raman spectra of the four anode sheets calculated by averaging all spectra recorded for the respective Raman map.

spectra presented in Fig. 7. The Raman spectrum of sample AB1 has a more intense D-band, while the average linewidth of the D-band is much larger than that found for the other samples. In addition, it seems that the band profile of the G-band is composed of two bands, one with a small linewidth having its maximum intensity around 1580 cm^{-1}, and a second, broader feature. Thus, it is obvious that sample AB1 contains two types of carbonaceous materials. Interestingly, spectra of all samples show well developed second-order bands, an observation which could be explained by the presence of well graphitized domains in the carbons.

At this point we were interested to see whether it is possible to detect differences between the Raman spectra of samples AB2–AB4, using the method proposed above for the cathode sheets. As the descriptor, we selected the correlation length L_a, which is derived by the relation given above. In fact, using the correlation length in an analysis of the Raman maps recorded for the anodes is equivalent to using an intensity ratio for the description of Raman maps.

In Fig. 8, histograms are presented that illustrate the distribution of the parameters L_a calculated for the anode samples investigated. Again a logarithmic scale was employed to enhance the small contributions to the histogram. The interval for the correlation lengths L_a is 5 nm. Two different types of distributions may be discerned: for anodes AB1 and AB4 the contributions are concentrated at small correlation lengths (less than 60 nm, with just one exception for AB4), whereas samples AB2 and AB3, which are very similar, have contributions from much larger correlation lengths L_a (up to 250 nm). In all cases a peak occurs in the distribution at low correlation lengths. The most symmetric distribution is obtained for the sample AB4.

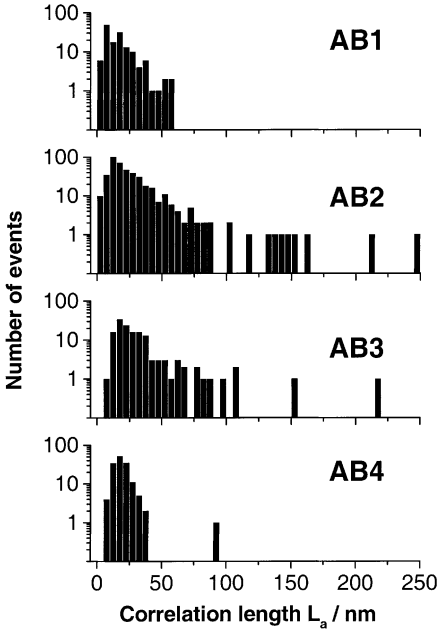

Fig. 8. Distributions of calculated correlation lengths L_a for four different anode sheets. The sampling interval in the histograms is 5 nm.

Table 2
Average correlation lengths L_a (nm) determined for the set of anodes investigated

Sample	Number-weighted average	Intensity-weighted average	Number of spectra included
AB1	16.6	9.1	144
AB2	27.2	18.7	420
AB3	33.9	23.5	196
AB4	19.3	18.8	196

The average correlation length calculated for this sample is the smallest in the set of values obtained for the anodes AB2–AB4 (Table 2). In addition, the difference between number-weighted average and intensity-weighted average is lowest for the sample AB4, a result that mirrors the narrow, symmetric distribution of correlation lengths. For all samples investigated, the intensity-weighted average value of L_a is smaller than the number-weighted average. This observation is interpreted in the sense that less-ordered carbon occurs at fewer locations on the electrode, but its signals provide a major contribution to the total signal recorded in the Raman map. The largest difference is observed for the sample AB1, which is the sample where even the averaged spectrum suggested that two types of carbon materials were employed in the formulation. From video micrographs (Fig. 6), it is known that the samples investigated contain at least two types of carbon. It has already been mentioned that the porosity of the carbon material strongly affects the amount of scattered light, and thus the recorded Raman intensity. The surface of the MCMB particles appears to be more porous, according to the micrographs. Thus, a tentative interpretation would correlate the difference between the number-weighted and intensity-weighted average with the amount of MCMB particles present at the anode surface. However, the heat treatment temperature used in the preparation of the MCMB particles has to be taken into account as well.

4. Conclusions

It was demonstrated in the present work that Raman microscopy is a fast and reliable characterization tool for practical electrodes of rechargeable lithium-ion batteries. The analysis of spectral features observed at a multitude of locations on the electrode surface yields a distribution of band parameters that is unique for a given kind of electrode. We show that band positions, linewidths, and intensity ratios can be employed as descriptors of the distribution. In turn, such distributions can be employed to generate a fingerprint for a particular kind of electrode.

Acknowledgements

We thank the Renata AG, Itingen, the Commission for Technology and Innovation, Bern, and Dr. O. Haas, Paul

Scherrer Institute for electrode samples, financial support, and numerous discussions, respectively.

References

[1] F. Tuinstra, J.L. Koenig, J. Chem. Phys. 53 (1970) 1126.
[2] R.J. Nemanich, S.A. Solin, Phys. Rev. B 20 (1979) 392.
[3] Y. Wang, D.C. Alsmeyer, R.L. McCreery, Chem. Mater. 2 (1990) 557.
[4] L. Nikiel, P.W. Jagodzinski, Carbon 31 (1993) 1313.
[5] Y. Kawashima, G. Katagiri, Phys. Rev. B 52 (1995) 10053.
[6] S. Solin, in: H. Zabel, S. Solin (Eds.), Graphite Intercalation Compounds, Vol. I, Springer, Berlin, 1990, p. 178.
[7] M. Inaba, Y. Iriyama, Z. Ogumi, Y. Todzuka, A. Tasaka, J. Raman Spectrosc. 28 (1997) 613.
[8] X. Zhang, R. Frech, J. Electrochem. Soc. 145 (1998) 847.
[9] J.-C. Panitz, F. Joho, P. Novák, Appl. Spectrosc. 53 (1999) 1188.
[10] P. Novák, F. Joho, R. Imhof, J.-C. Panitz, O. Haas, J. Power Sources 81/82 (1999) 212.
[11] I. Rey, J.C. Lassègues, P. Baudry, H. Majastre, Electrochim. Acta 43 (1998) 1539.
[12] J.-C. Panitz, Appl. Spectrosc. 51 (1997) 1073.
[13] M. Inaba, H. Yoshida, Z. Ogumi, T. Abe, Y. Mizutani, M. Asano, J. Electrochem. Soc. 142 (1995) 20.